Biosensors and Bioelectronics 146 (2019) 111733

Contents lists available at ScienceDirect

Biosensors and Bioelectronics

journal homepage: http://www.elsevier.com/locate/bios

Controllably prepared molecularly imprinted core-shell plasmonic nanostructure for plasmon-enhanced fluorescence assay

Hui He, Pir Muhammad, Zhanchen Guo, Qiling Peng, Haifeng Lu, Zhen Liu *

State Key Laboratory of Analytical Chemistry for Life Science, School of Chemistry and Chemical Engineering, Nanjing University, Nanjing, 210023, China

ARTICLE INFO

Keywords:
Nanoparticles
Molecularly imprinted polymers
Plasmon-enhanced fluorescence
Boronate affinity
Controllable synthesis

ABSTRACT:

Plasmon-enhanced fluorescence (PEF) is an emerging technology for sensitive detection. It relies on the plasmonic effect of a noble metal nanostructure to dramatically enhance the fluorescence of target fluorophores around the metal surface. Because there is a compromise between plasmonic enhancement and fluorescence quenching, it is critical to control the distance between the fluorophore and the metal surface to an appropriate range. This makes the fabrication of plasmonic nanostructures for PEF assays a challenging task. Herein, we report a controllably prepared core-shell plasmonic nanostructure coated with molecularly imprinted polymer (MIP) for sensitive and specific PEF assay. Riboflavin (RF) was used as a test compound in this study. RF-imprinted Ag@SiO_2 nanoparticles were prepared in a controllable manner, providing an optimal distance between the metal surface and RF molecules. The obtained hybrid nanostructure allowed for sensitive detection and specific recognition towards the target. Based on the plasmonic hybrid nanostructure, a sensitive and specific PEF assay of RF was developed and successfully applied to the determination of RF in human urine. Thus, the study paved the way for controllable preparation of molecularly imprinted plasmonic nanostructures for sensitive and specific PEF assays.

1. Introduction

Plasmon-enhanced fluorescence (PEF)-based biosensing has been recently developed as a promising technique for the detection of biomolecules in diverse fields such as medical diagnosis, biological monitoring and food security (Geddes and Lakowicz, 2002; Aslan et al., 2005; Bauch et al., 2014; Punj et al., 2015; Holzmeister et al., 2014). PEF relies on remarkable plasmonic properties of noble metal nanostructures originating from localized surface plasmon resonance (LSPR) by incident light and the interaction between fluorophores and surface plasmons to dramatically enhance emitted fluorescence intensity, enabling sensitive detection of target fluorophores around the metal surfaces. The design and fabrication of plasmonic nanostructures are essential to the performance of developed PEF assays, for which two aspects are crucial. One is the distance between the fluorophore and the plasmonic nanostructure, which dramatically influences the sensitivity. When the fluorophore and the plasmonic nanostructure are too close, fluorescence quenching occurs (Bauch et al., 2014; Cannone et al., 2006; Li et al., 2017); whereas when the distance is too far, fluorescence signal is weak due to degenerative plasmon effect in the far field (Bauch et al., 2014; Li et al., 2017). Appropriate distance was reported to range from several to tens of nanometers (Bauch et al., 2014; Abadeer et al., 2014). Due to distinct properties of the fluorophore and the plasmonic nanostructure, the distance requires optimization by experiments. Thus, it is critical to precisely control the distance to an appropriate range, but this is challenging. The other is the specificity of fabricated PEF sensors towards target molecules. This is critically important for complex biological samples because there are a huge number of high-abundance interfering compounds coexisting in the samples.

To enhance the sensitivity of PEF-based biosensors, a variety of metallic nanostructures with well-defined topology and dimensions have been prepared, such as nanoclusters (Touahir et al., 2010; Xu et al., 2011; Volpati et al., 2008) and nanoparticles (NPs) (Bharadwaj and Novotny, 2007, 2010; Schmelzeisen et al., 2010; Ming et al., 2009; Kinkhabwala et al., 2009; Brolo et al., 2005). Particularly, silica-encapsulated metal NPs have shown great potential as a useful means to mediate the distance between fluorophores and metal surfaces. Abadeer et al. (2014) fabricated silica shell-encapsulated gold nanorods to amplify the fluorescence signal of an infrared dye. They demonstrated that the fluorescence response strongly depended on the thickness of the

* Corresponding author.
E-mail address: zhenliu@nju.edu.cn (Z. Liu).

https://doi.org/10.1016/j.bios.2019.111733
Received 2 August 2019; Received in revised form 24 September 2019; Accepted 26 September 2019
Available online 1 October 2019

silica shell. Besides, Bardlan et al. (2008) prepared a silica epilayer on AuNPs to enhance near-infrared fluorescence of indocyanine green. However, the silica thickness was uncontrollable during the synthesis procedures in these works. To gain recognition specificity for PEF assays, on the other hand, aptamers (Zhou et al., 2014a,b; Li et al., 2011; Park et al., 2017; Zhou et al., 2014a,b; Niu et al., 2017) and antibodies (Aslan et al., 2005; Dostalek and Knoll, 2008) have been the main ligands to fabricate plasmonic nanostructures. Overall, aptamers and antibodies provide good specificity and can function as a spacer to keep the fluorophores from the metal surface to a certain distance. However, aptamer or antibody-modified plasmonic metallic nanostructures are associated with several disadvantages including uncontrollability and poor stability. Therefore, it is of great interest to exploit versatile and controllable plasmonic nanostructures with maximum signal enhancement and high specificity.

Molecularly imprinted polymers (MIPs), which are tailor-made biomimetic receptors synthesized through polymerization in the presence of a template, have developed into important functional materials with antibody-like binding properties (Vlatakis et al., 1993; Whitcombe et al., 2011; Chen et al., 2016a,b; Liu and He, 2017). Due to their intrinsic features of stability, specificity and reusability, MIPs have found a wide range of important applications such as separation (Adbo and Nicholls, 2001; Wang et al., 2003; Chen et al., 2016a,b), sensing (Ye and Mosbach, 2001; Wan et al., 2013; Bai and Spivak, 2014; Bhogal et al., 2019; Chen et al., 2018; Gao et al., 2014; Li et al., 2018; Tian et al., 2015; Wang et al., 2018; Yang et al., 2018), disease diagnosis (Li et al., 2013; Ye et al., 2014; Muhammad et al., 2017), and drug delivery (Canfarotta et al., 2018). As chemically synthesized alternatives of antibodies and aptamers, MIPs can be promising parts to be integrated into advanced plasmonic nanostructures for sensitive and specific PEF assays. Ton et al. (2013) demonstrated a MIP-based fiber-optic fluorescence sensor with enhanced sensitivity by AuNPs. However, to our best of knowledge, there have been no other reported MIP-integrated PEF assays so far. A major reason seems to be the difficulty in controlling the distance between fluorophores and metal surfaces.

Recently, our group has developed several controllable molecular imprinting approaches (Wang et al., 2014; Bie et al., 2015, 2018; Xing et al., 2017, 2019), which allowed for facilely producing desirable imprinting layer thickness through adjusting the imprinting time. The prepared MIPs exhibited excellent binding properties towards a large variety of biomolecules such as proteins, peptides, glycans, and monosaccharides, enabling a range of promising applications including proteomic analysis (Bie et al., 2015), disease diagnosis (Li et al., 2019; Tu et al., 2016; Bi and Liu, 2014), single cell analysis (Liu et al., 2016), cancer imaging (Yin et al., 2015; Wang et al., 2016) and cancer therapy (Yin et al., 2017; Dong et al., 2019). Particularly, the sol-gel based

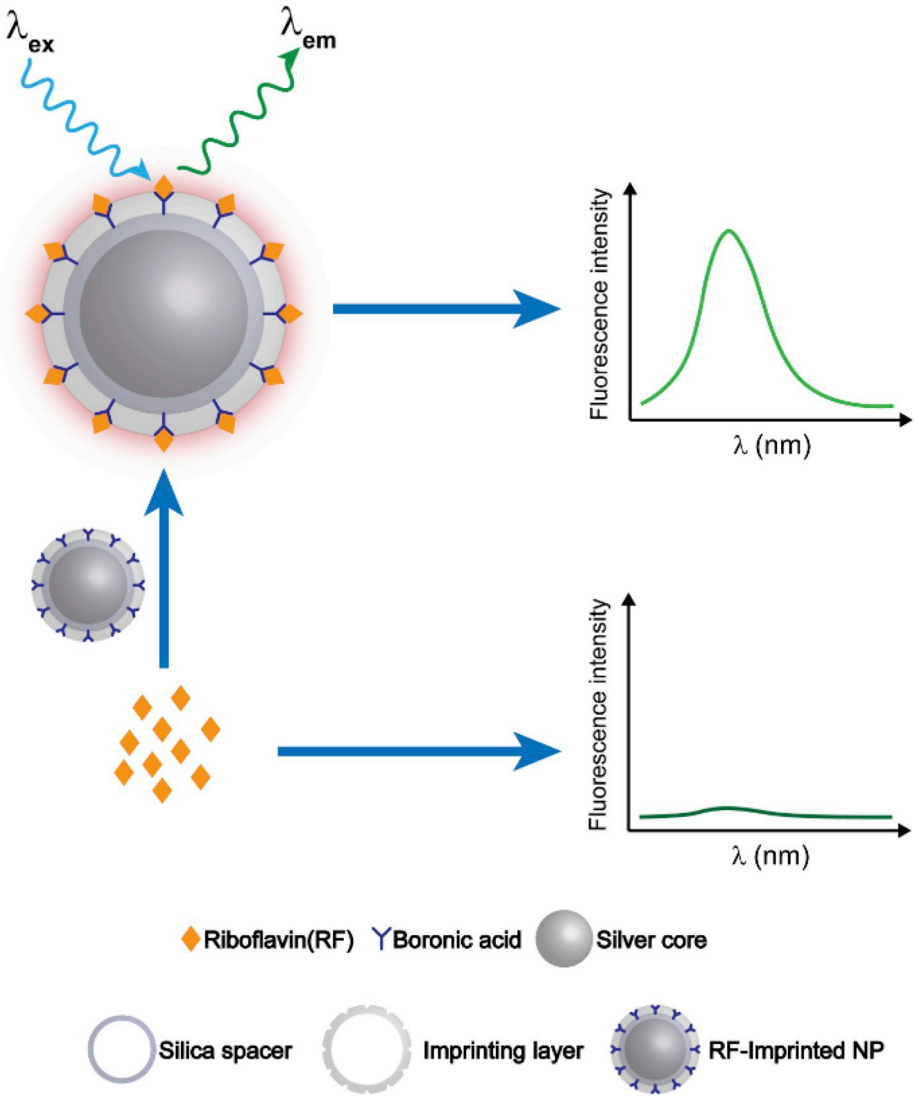

Scheme 1. Schematic of the plasmon enhanced fluorescence assay based on molecularly-imprinted core-shell Ag@SiO_2 NPs.

boronate affinity controllable oriented surface imprinting approaches (Bie et al., 2015, 2018; Xing et al., 2017) exhibited great potential for controllable nanoscale fabrication of MIPs. It even allowed for precise controlling the thickness of imprinting layer (Bie et al., 2018). This highly desirable controllability inspired us to explore the possibility to fabricate advanced plasmonic nanostructures for PEF assays though controllable molecular imprinting.

Herein, we report a controllably prepared core-shell Ag@MIP hybrid plasmonic nanostructure for sensitive and specific PEF assay. As a proof-of-the-principle, riboflavin (RF) or vitamin B_2, which plays significant roles in human body, was used as a test compound in this study. RF-imprinted Ag@SiO_2 NPs were prepared in a controllable manner. The effects of core size and shell thickness was investigated and optimized. The obtained plasmonic MIPs were employed to establish a sensitive and specific PEF assay of RF. The MIP-based PEF assay is illustrated in Scheme 1. RF molecules from a sample solution are first specifically captured by RF-imprinted Ag@SiO_2 NPs. After removal of unbound RF molecules and interfering species in the sample, the solution containing RF-bound Ag@MIP NPs is subject to fluorescence detection. Under radiation of laser, the fluorescence signal from RF on the imprinted Ag@SiO_2 NPs is dramatically enhanced through surface plasmons on the nanoparticles. The experimental results indicated that the silica shell thickness of the hybrid plasmonic nanostructure can be facilely controlled to provide an optimal distance between metal surface and RF molecules. Finally, the MIP-based PEF assay was successfully applied to the determination of RF in human urine. Thus, the study paved a sound basis for controllable preparation of molecularly imprinted plasmonic nanostructures for sensitive and specific PEF assays.

2. Material and methods

2.1. Chemicals and materials

Flavin mononucleotide (FMN) and nicotinamide adenine dinucleotide (NADH) were purchased from Sigma Aldrich (St. Louis, MO, USA). L-Tyrosine and L-tryptophan were purchased from J&K Chemical (Shanghai, China). Pyridoxine (VB6), folic acid (VB9) and coenzyme B12 (VB12) were obtained from Aladdin Chemical (Shanghai, China). 3-Aminopropyltriethoxysilane (APTES, 98%) and tetraethylorthosilicate (TEOS, 99%) were purchased from Sigma Aldrich (St. Louis, MO, USA). Riboflavin (RF, 97%), sodium cyanoborohydride (95%) and 4-formylphenylboronic acid (FPBA) were obtained from J&K Chemical (Shanghai, China). Ammonia water (28%, v/v) and acetonitrile were purchased from Sinopharm Chemical Reagent (Shanghai, China). Sulfuric acid (98%), hydrogen peroxide (30%), potassium bicarbonate ($KHCO_3$), trisodium citrate and hydrochloric acid (36%) were purchased from Shanghai Lingfeng Chemical Reagent (Shanghai, China). Glacial acetic acid (HAc), sodium dihydrogen phosphate (NaH_2PO_4), disodium hydrogen phosphate (Na_2HPO_4), and anhydrous ethanol/methanol were purchased from the Nanjing Reagent Company (Nanjing, China). All of the chemical reagents were of analytical grade unless otherwise specially noted. These reagents were used without further purification. Additionally, water used in our experiments was purified by a Milli-Q Advantage A10 ultrapure water purification system (Millipore, Milford, MA, USA). Glass slides (75 mm × 25 mm) were purchased from the Shanghai Machinery Import and Export Corporation (Shanghai, China).

2.2. Instruments

Transmission electron microscopic (TEM) characterization was carried out on JEOL JEM-2800 instrument (Tokyo, Japan). Scanning electron microscopic (SEM) characterization was performed on JSM-7800F instrument (Tokyo, Japan). The evaluation of particle size and distribution was performed on a BI-200SM dynamic light scattering (DLS) machine (Brookhaven Instrument, Holtsville, USA). Nitrogen adsorption-desorption isotherms were obtained on a Quantachrome Autosorb-IQ-2C analyzer at 77 K. Specific surface areas and pore size distributions were measured by the Brunauer-Emmett-Teller (BET) and Barrett-Joyner-Halenda (BJH) methods, respectively. Fluorescent properties of the prepared NPs as well as free RF in bulk solution were characterized on an F-7000 fluorescence spectrometer (Hitachi, Tokyo, Japan). Evaluation of boronic acid-functionalization and molecular imprinting was performed on a Synergy Mx microplate reader from BioTek (Winooski, VT, USA). UV-vis extinction spectra were recorded on UV-1800 spectrophotometer (Shimadzu, Kyoto, Japan). Surface enhanced Raman scattering (SERS) measurements were implemented on a Renishaw InVia Reflex confocal Raman microscope (Renishaw, UK), which was equipped with a high-resolution grating (1800 grooves/mm) and thermodynamically cooled charge-coupled device (CCD) detector. A He-Ne laser with excitation source ($\lambda_0 = 633$ nm; laser power at a spot, 17 mW) was applied. The acquisition time was 1 s.

2.3. Finite-difference time domain (FDTD) simulations

All FDTD simulations were undertaken using the software Lumerical FDTD Solution (Vancouver, Canada). The Ag core was modeled as a sphere with different diameters ranging from 40 nm to 110 nm, and the refractive index was taken from the material database of CRC. The Ag core coated with SiO_2 spacer layer of different shell thicknesses (0–35 nm). In all cases, total-field/scattered-field light source conditions were used. The incident light injected toward -*z* direction, and polarized along x-axis. The incident wavelength was set as 450 nm. The incident field was defined as a plane wave with a wave-vector that is normal to *x*-*y* plane. The simulation region was set to 200 × 200 nm^2 with highly accurate mesh step of d*x*=d*y*=d*z*=0.5 nm for each simulation.

2.4. Synthesis of AgNPs

AgNPs (60 nm in core size) were prepared as described by Lee and Meisel (1982). In brief, $AgNO_3$ (36 mg) was dissolved in 200 mL water and brought to boil under continuous stirring. Then, 4 mL of 1% (w/v) trisodium citrate was added. The mixture was boiled with stirring for about 1 h and then cooled down to room temperature naturally. The solution was stored at 4 °C before use.

2.5. Synthesis of silica NPs

Silica NPs were prepared according to a previously reported method (Wang et al., 2016) with modifications. In brief, both precursors, i.e., APTES (12 μL APTES and 2 mL ethanol) and TEOS (0.48 mL TEOS and 6.4 mL ethanol), were mixed together. Afterwards, a known volume of ethanol (64 mL) was mixed with 3.88 mL water and 2.88 mL ammonium water in a round-bottom flask and then was heated slowly up to 55 °C under vigorous agitation, followed by a rapid addition of the previously prepared precursor solution. After 3 h of airtight reaction, the prepared silica NPs was collected via centrifugation (11000 rpm × 15 min). The prepared NPs were rinsed with ethanol and water for two times and dispersed into ultra-pure water to store at room temperature for further use.

2.6. Preparation of Ag@SiO_2 hybrid nanostructure

To cap a silica shell onto the surface of AgNPs, a procedure described by Baida and co-workers (Baida et al., 2009), was employed with modifications. A volume of 40 mL of ethanol was added to 10 mL of Ag colloidal solution with stirring. Subsequently, a volume of 0.7 mL of ammonia solution (28%) was dropwise added to the suspension, and the mixture was stirred for 5 min. Then 20 μL of 10 mM TEOS dissolved in ethanol was added to the suspension. The reaction mixture was slowly stirred at room temperature for different durations. The thickness of the silica shell was adjusted to desired value by varying the reaction time. After that, the as prepared Ag@SiO_2 NPs were centrifuged at 10,000 rpm

for 15 min and washed with ethanol three times, then dispersed in 10 mL of anhydrous ethanol for further use.

2.7. Preparation of RF-imprinted silica NPs and Ag@SiO_2 NPs

Molecular imprinting on the surface of silica NPs and Ag@SiO_2 NPs was realized by previous methods (Bie et al., 2015; Xing et al., 2017). The procedure of imprinting is schematically illustrated in Scheme S1, which included four major steps: 1) boronic acid functionalization, 2) template immobilization, 3) oriented imprinting, and 4) template removal. Briefly, amino groups were introduced by adding 100 μL of APTES to 10 mL of anhydrous ethanol solution containing freshly synthesized Ag@SiO_2 NPs, then the mixture was stirred for 1.5 h. The resultant amino-modified Ag@SiO_2 NPs were then isolated by centrifugation. Afterwards, they were dispersed in 30 mL ethanol. Then, 300 μL of 5 mg/mL FPBA and 100 μL of 1 mg/mL sodium cyanoborohydride were added into 30 mL of amino-modified Ag@SiO_2 NPs suspension. After reaction for 24 h, the solution was centrifuged at 8,000 rpm for 10 min and the boronic acid-functionalized Ag@SiO_2 NPs were precipitated from solution, and washed with ethanol and water for three times. Finally, the boronic acid-functionalized Ag@SiO_2 NPs were dispersed in 10 mL water. For template immobilization, 1 mL of 1 mg/mL RF dissolved in 100 mM of phosphate buffer (pH 7.4) was added into the solution of boronic acid-functionalized Ag@SiO_2 NPs and the pH was adjusted to 7.4. After incubation for 30 min, RF-bound NPs were obtained by centrifugation at 8,000 rpm and washed with phosphate buffer (100 mM, pH 7.4) for two times. For oriented imprinting, the RF-immobilized boronic acid-functionalized Ag@SiO_2 NPs were redispersed by 40 mL ethanol, added stepwise with 0.7 mL ammonium water and a prepolymer solution that was consisted of 22.4 μL TEOS and 10 mL ethanol. During a typical imprinting process, functional monomers surrounding the RF molecules were polymerized, thereby ensuring the imprinted site within the polymer. After reaction for an appropriate duration, the reacting mixture was centrifuged and the precipitates were collected. For template removal, the sediments were washed with 0.1 M HAc with 10% acetonitrile (v/v) for 2.5 h and template molecules can be completely eliminated from the MIPs layer, thereby exposing the imprinted sites. Ultimately, the RF-imprinted NPs were obtained via centrifugation process at 8,000 rpm for 8 min and washed with phosphate buffer (pH 7.4) for two times each; finally, the collected precipitates were stored in water for further use. To prepare non-imprinted polymer on silica NPs and Ag@SiO_2 NPs for comparison, the procedure was almost the same without addition of RF template.

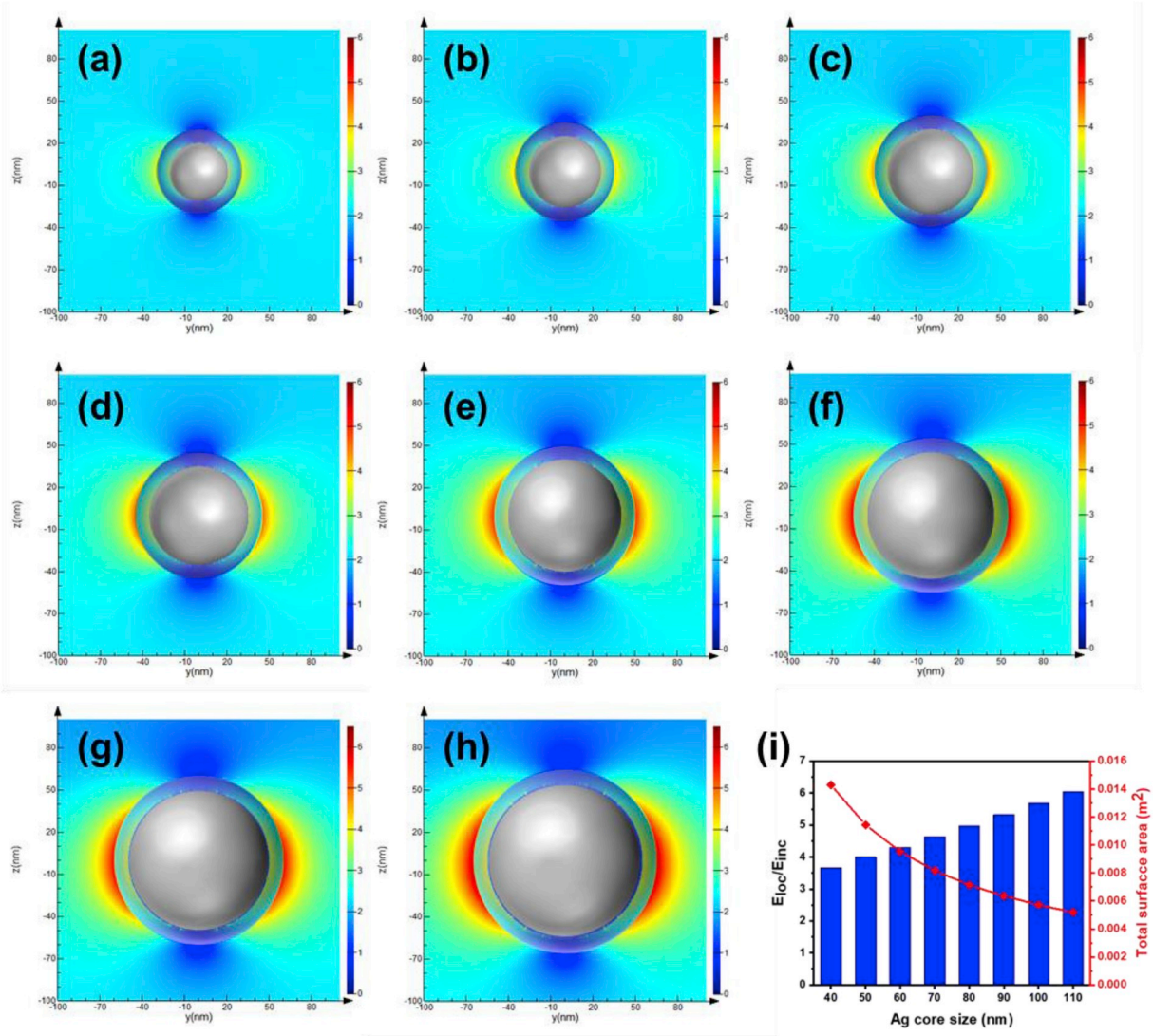

Fig. 1. FDTD simulations of E-field on the surface of Ag@SiO_2 NPs of different core size. Core size: (a) 40 nm, (b) 50 nm, (c) 60 nm, (d) 70 nm, (e) 80 nm, (f) 90 nm, (g) 100 nm, (h) 110 nm; the thickness of the silica shell: 10 nm; (f) Dependence of the localized E-field enhancement (E_{Loc}/E_{Inc}) within the dotted square at the surface of silica shell on the core size. The mass of AgNPs was set as 1 mg for calculating the total surface area.

3. Result and discussion

3.1. Simulation of effects of the core size

The electric (E) field redistribution can be an indicator of signal intensity in various kinds of plasmon-enhanced spectroscopy when a laser beam irradiates on NPs (Bauch et al., 2014). Invariably, the enhancement of PEF can be analogously confirmed by E-field distribution on plasmonic metal substrates, which can give insight into the PEF mechanism. For this purpose, FDTD simulation was chosen as an effective tool to portray the E-field's spatial distribution around the irradiated NPs of arbitrary shape by numerical calculation of Maxwell's equations. Owing to its versatility and flexibility in simulation, FDTD simulation allows for quantification of the E-field distribution around the Ag@SiO_2 NPs in this study. Firstly, a survey of the effect of spherical Ag core on the E-field enhancement E_{loc}/E_{inc} was carried out. E_{inc} and E_{loc} are the incident and localized E-field around the NPs, respectively. Fig. 1 presents contours of the E-field enhancement E_{loc}/E_{inc} around the spherical Ag@SiO_2 hybrid structures with different core sizes, and the values of E_{loc}/E_{inc} indicate the contribution of E-field enhancements to the PEF intensity. In principle, the PEF enhancement factor (EF) can be simply expressed as $(E_{loc}/E_{inc})^2$ on the metal NPs (Bauch et al., 2014; Baida et al., 2009). In order to investigate the effects of AgNPs core size on E-field enhancement, we simplified the models by fixing the silica shell of the Ag@SiO_2 NPs at 10 nm. An incident beam of 450 nm propagated along -*z*-axis in the FDTD-simulations. Fig. 1a–h shows that the localized E-fields on the hybrid structures trended to favorably concentrate at the surfaces of both Ag matrix and silica shell, stimulating the hot spots of PEF. To precisely inspect PEF intensity's response to AgNPs core in Ag@SiO_2 hybrid structures, a straightforward method is to monitor E-field change on the boundary between the silica shell and environment where the fluorophores are anchored. As shown in Fig. 1, the localized E-field at the surface of silica increased by several times with respect to that of the E_{inc}. Fig. 1i summarizes the maximum E_{loc}/E_{inc} values on the boundary between the silica shell and environment of each Ag@SiO_2 model. The E_{loc}/E_{inc} value increased linearly as increasing the core size of Ag@SiO_2 NPs. Clearly, a larger Ag core is more favorable for fluorescence enhancement, but results in reduced specific binding capacity due to its lower specific surface area. To balance the fluorescence enhancement and binding capacity, therefore, we chose the 60 nm of core size in further investigations.

3.2. Optimization of imprinting time

The effect of imprinting time was evaluated in terms of the imprinting factor (IF), which is defined as the ratio of the signal intensity for the template captured by the imprinted material over that by the non-imprinted material under otherwise identical conditions. Fig. S1 shows the dependence of imprinting factor on imprinting time. The optimal imprinting time was found to be 25 min, giving a maximum IF value of 15.2, which is outstanding in the field of molecular imprinting. According to the linear thickness-imprinting time dependence established previously ($l = 0.51 + 0.04 \times t$, $R^2 = 0.994$, l is thickness in nm and t is imprinting time in min) (Bie et al., 2015), the thickness of the imprinting layer obtained at the optimal imprinting time was estimated to be 1.51 nm. Based on the molecular structures, the length of single RF molecule and boronic acid-functionalized part was estimated by ChemBio 3D to be 0.60 and 1.17 nm, respectively. Thus, the coverage of the imprinting layer on the template and ligand was roughly estimated to be 85.3%, suggesting that most part of the immobilized template molecule was embedded in the imprinting layer. After the template removal, the cavity complementary to templated molecular shape formed on the surface. Note that the thickness of imprinting layer must be controllable. When the thickness exceeding the length of template and ligand, the template was not be removed; on the other hand, too thin imprinting layer was not able to complete remember the molecular shape, reducing the imprinting performance (Wang et al., 2014; Bie et al., 2015, 2018; Xing et al., 2017, 2019).

3.3. Optimization of template removal time

The template removal time was optimized through monitoring the residual template molecules within the imprinted material after being washing with the template removing solution for different time. Fig. S2 shows the dependence of the fluorescence intensity for RF remained on the imprinted Ag@SiO_2 NPs on template removal time. The intensity decreased gradually as the template removal time exceeded within initial 2.5 h, but remained unchanged afterwards. This suggests that washing with the selected solution for 2.5 h allowed for complete removal of the template from the MIP. Thus, 2.5 h was selected for the template removal in later experiments.

3.4. Effect of the silica shell on PEF

As a prerequisite for the PEF assay, the target molecules must be fluorescently active. Riboflavin is one of prominent members of the flavins, which serves as a fluorophore. Fig. 2a gives the absorption and emission spectra for RF in 100 mM phosphate buffer (pH 7.4). The absorbance band exhibited two typical peaks at 375 and 450 nm, corresponding to the singlet S2 and S1 excited states of RF (Li et al., 2015; Tachibana, 1971). The fluorescence emission peak appeared at 530 nm. To verify the plasmonic enhancement effect, we firstly investigated the native fluorescence response of RF in the presence of bare AgNPs without any silica shell. Fig. 2b shows fluorescence spectra for RF solutions of identical concentration with and without the presence of different NPs. Free RF in aquous solution emitted weak fluorescence. When AgNPs were present in the solution of RF, the fluorescence was completely suppressed. This was because that direct contact of fluorophores and bare AgNPs resulted in quench of the fluorescence emission. When RF-imprinted silica NPs were added to the solution of RF, the fluorescence was slightly enhanced. Although the mechanism of this enhancement is unclear at present, the slight fluoresence enhancement effect of the silica NPs should be taken into account for later quantitative investigation of the effect of plasmonic core on the fluorescence. As a contrast, the RF-imprinted Ag@SiO_2 NPs were present in the solution of RF, the fluorescence was significantly enhanced (by 27.6-fold). As compared with the case with the presence of RF-imprinted SiO_2 NPs, the fluorescence intensity at the presence of RF-imprinted Ag@SiO_2 NPs was enhanced by 8.1 folds. This indicates that the designed core-shell imprinted Ag@SiO_2 NPs were effective to enhance the fluorescence of the fluorophore.

To elucidate the effect of the silica shell thickness on PEF, we theoretically and experimentally investigated a series of shell thickness spanning from 0 to 35 nm. By using the FDTD approach, we further estimated the E-fields on the boundary between the silica shell and environment. A representative simulation at the silica thickness of 15 nm is shown in Fig. 2c. With the estimated values for E_{loc}/E_{inc}, the estimated enhancement factors for different silica shell thicknesses, which are expressed as $(E_{loc}/E_{inc})^2$, were calculated. The obtained enhancement factors were plotted against the shell thickness, as shown in Fig. 2d. The estimated enhancement factor reached a maximum when the shell thickness was 13.6 nm. Experiments for the measurement of PEF enhancement factor were carried out on the same shell thicknesses. Considering the slight enhancement effect of silica NPs, the experimental enhancement factors were normalized by RF-imprinted silica NPs; that is, the experimental enhancement factors were the ratio of the fluorescence intensity at the presence of RF-imprinted Ag@SiO_2 NPs over that at the presence of RF-imprinted silica NPs under otherwise identical conditions. As shown in Fig. 2d, the experimental measurements gave a maximum enhancement at the shell thickness of 15 nm. Clearly, the estimated and experimental optimal shell thicknesses were very close, indicating the nanoscale fabrication process in this study was

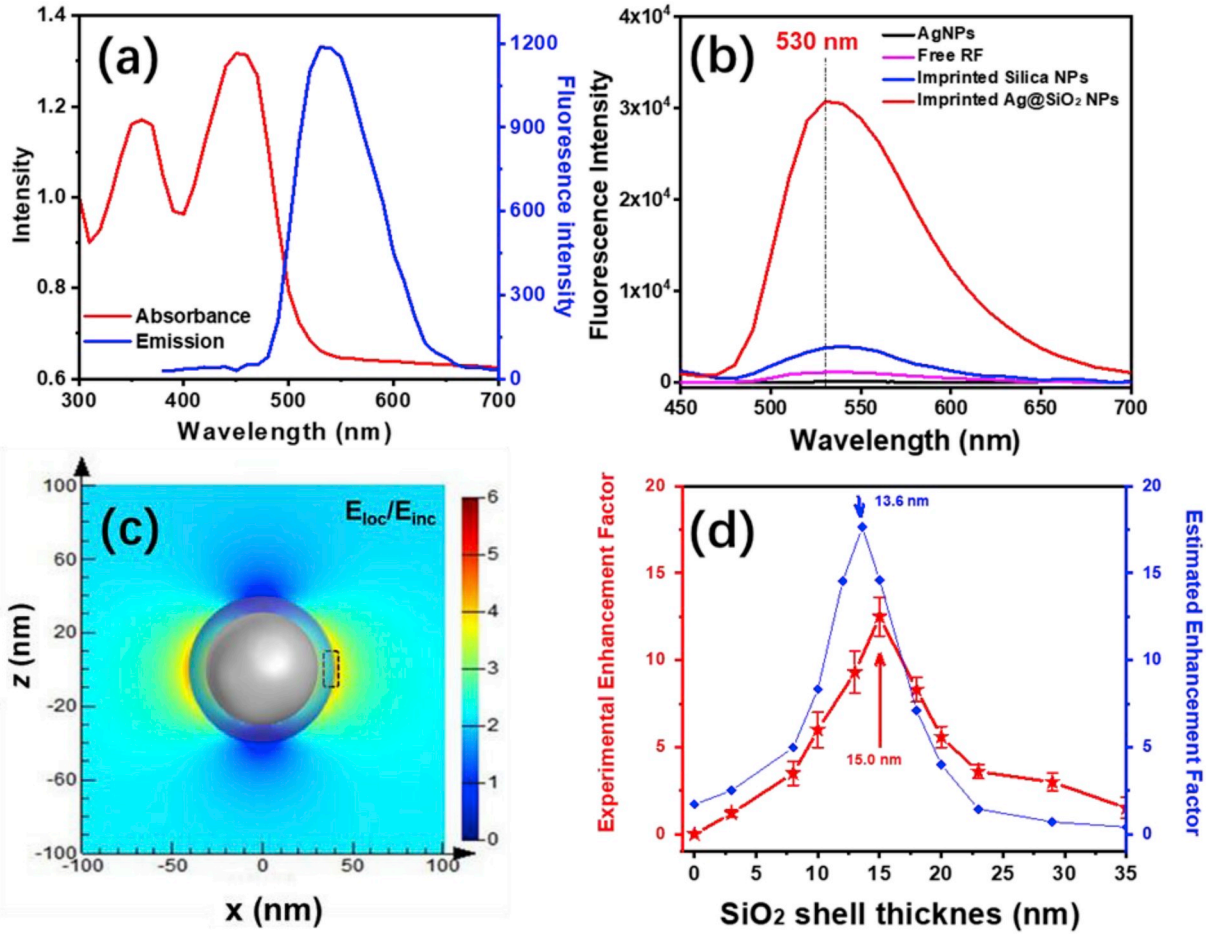

Fig. 2. (a) The absorption and emission spectra for RF in 100 mM phosphate buffer (pH 7.4). (b) Comparison of fluorescence spectra for RF in solution with and without the presence of different NPs. (c) FDTD-calculated electrical field intensity at the surface of Ag@SiO_2 NPs with a 60 nm core size and a 15 nm silica thickness. Dotted square indicates the area used for the calculation of electric field enhancement factor. (d) Dependence of experimental PEF enhancement factor and calculated electric field enhancement factor on the thickness of the silica shell. Sample: RF (1 μg/mL dissolved in 100 mM phosphate buffer, pH 7.4) and 200 μL RF-imprinted Ag@SiO_2 solution. Experiments were performed in triplicate; errors bars represent standard deviations. The experimental PEF enhancement factor was calculated through normalization of each fluorescence emission intensity by that of MIP on silica NPs under identical conditions.

well controlled. Based on above results, 15 nm silica shell was used for later experiments unless specially mentioned.

3.5. Characterization of RF-imprinted Ag@SiO_2 NPs

The morphology and size of the resultant AgNPs and Ag@SiO_2 NPs were characterized by high resolution TEM. As shown in Fig. S3a, the bare spherical AgNPs exhibited a monodispersed size, with an average diameter of 60 nm. Figs. S3b–3d show the TEM images of well-dispersed spherical Ag@SiO_2 NPs with different SiO_2 shell thickness of 8, 15, and 35 nm, respectively. It has been already established that, under well-controlled conditions, the thickness of silica shell produced by the hydrolysis of TEOS in ethanol increased linearly with polymerization time, growing at the rate of 0.04 nm per minute ($d = 0.04t + 0.51$) (Bie et al., 2015). To obtain desired thickness, the polymerization time was controlled. As a comparison, spherical silica NPs, which were synthesized as a control, showed an average diameter of 60 nm from the TEM image (Fig. S4). The RF-imprinted and non-imprinted Ag@SiO_2 NPs were also characterized by scanning electron microscopy (SEM), TEM and energy dispersive X-Ray spectroscopy (EDX). Fig. S5 shows uniform imprinted and non-imprinted Ag@SiO_2 NPs with an average diameter of 90 nm. Fig. 3a also demonstrates uniform imprinted NPs with an average diameter of 90 nm. Fig. 3b–d shows that silica shell was successfully coated on AgNPs. Fig. 3e and f demonstrates the amine group and boronic acid ligand was modified on the surface of silica shell. Fig. 3g illustrates Si, O, N and B elements were modified on the surface of AgNPs. Intensity of all elements is shown in Fig. 3h. Fig. S6 shows corresponding characterization of non-imprinted Ag@SiO_2 NPs.

The sizes of as-prepared NPs, RF-imprinted and non-imprinted NPs on both silica and Ag@SiO_2 NPs were also confirmed by DLS analysis. As shown in Fig. S7, the NPs in all stages had good dispersibility and homogeneity in the narrow size distribution. Moreover, aggregation did not occur in solution. Based on DLS analysis, the average diameter of the spherical silica NPs was found to be 63 ± 8 nm, while diameters of the RF-imprinted and non-imprinted silica NPs were estimated to be about 92 ± 10 nm as shown in Figs. S7a–7c. Figs. S7d–7f indicate that the average diameter of the silver core was about 62 ± 5 nm; while RF-imprinted and non-imprinted Ag@SiO_2 NPs were estimated to be 93 ± 9 nm, suggesting a silica shell of ca. 15 nm thickness was successfully prepared on the AgNPs. Subsequently, transmission mode extinction measurements were performed. It was found that as the silica shell thickness increased, the wavelength of the maximum LSPR peak red-shifted (Fig. S8), which indicates that the silica shell thickness was well controlled.

The textural and surface properties of RF-imprinted and non-imprinted NPs were evaluated by BET and BJH analysis. Fig. S9a shows that RF-imprinted NPs exhibited a slightly better adsorption performance, meanwhile Table S1 indicates that RF-imprinted NPs possessed a larger surface area (144 m^2/g) as compared with non-imprinted NPs (85 m^2/g). The higher nitrogen adsorption ability and

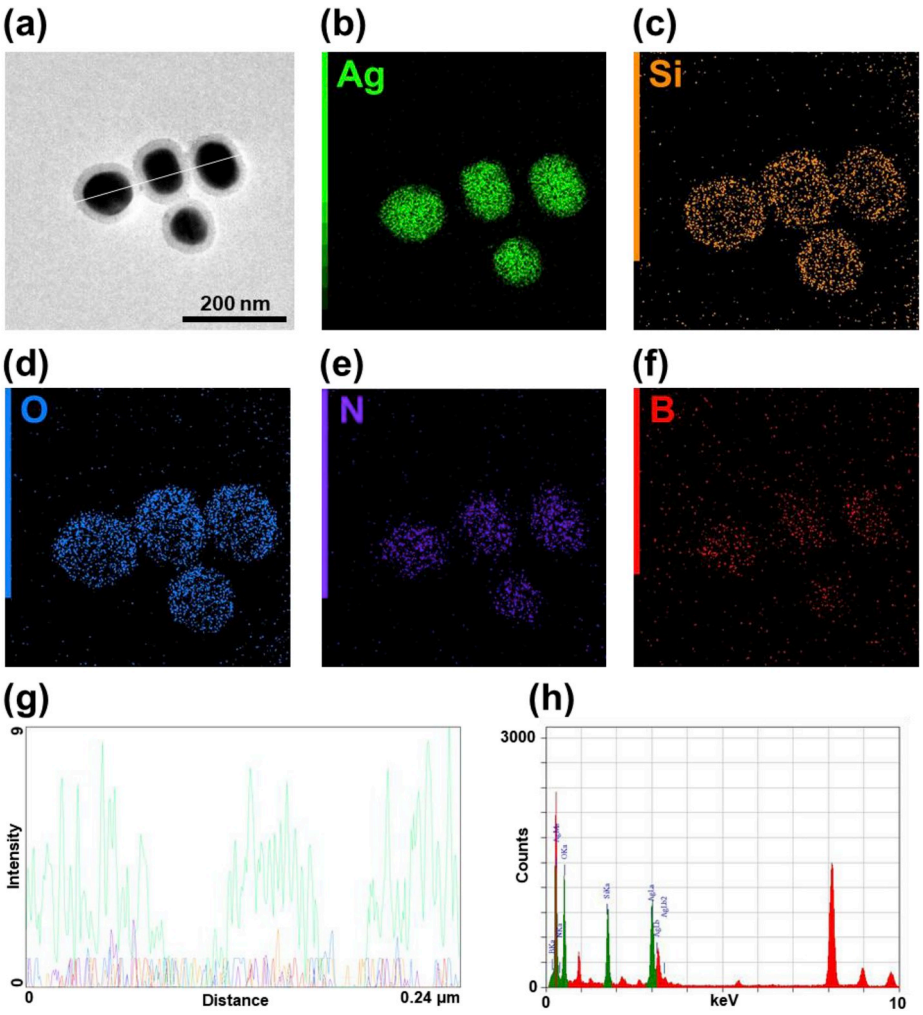

Fig. 3. TEM and EDX characterization of RF-imprinted Ag@SiO_2 NPs. (a) TEM image of RF-imprinted Ag@SiO_2 NPs. (b–f) Element distribution of RF-imprinted Ag@SiO_2 NPs, including Ag, Si, O, N and B. (g) Element distribution on the white line shown in (a). (h) Energy spectrum of all elements.

surface area of imprinted NPs can be attributed to the presence of imprinted cavities. Fig. S9b and Table S1 indicate that imprinted and non-imprinted NPs possessed similar porosity, pore volume and average pore diameter. Although the BET and BJH analysis reported the presence of pores of c.a. 20 nm on both imprinted and non-imprinted NPs, this can be assinged to the gap between deposited NPs rather than the imprinted cavities because the latter was much smaller in size (< 1 nm).

To confirm whether the target molecules adhere to the imprinted particles in close contact with the silica layer, we investigated fluorescence enhancement under different environmental pH. As shown in Fig. S10, at a high environmental pH, the combination of boronate affinity and shape matching in imprinted cavity provides a high affinity to target, enabling a stronger fluorescence enhancement; while at a low environmental pH, the boronate affinity interaction is disrupted and shape matching provides a moderate affinity, showing a reduced fluorescence enhancement. The boronate affinity interaction can be controlled by environmental pH (Li et al., 2015; Liu and He, 2017), thus the MIPs produced by boronate affinity-based oriented surface imprinting can capture the targets in a tunable mode. High fluorescence enhancement was obtained due to boronate affinity interaction, showing that the target molecules adhere to the imprinted particles in close contact with the silica layer through formation of boronate ester bond.

3.6. Characterization of imprinting effect

Binding isotherms, which are the plot of the amount of target captured by an absorbent against the initial target concentration in the solution which the absorbent is incubated with, were investigated for RF-imprinted and non-imprinted Ag@SiO_2 NPs. As shown in Fig. 4a, the imprinted Ag@SiO_2 NPs exhibited a distinctly different binding isotherm from the non-imprinted Ag@SiO_2 NPs. For the imprinted Ag@SiO_2 NPs, the bound amount increased apparently with the concentration of RF in the solutions when the concentration was lower than 0.5 μg/mL, but a plateau was reached after the concentration exceeded 0.5 μg/mL. As a comparison, for the non-imprinted Ag@SiO_2 NPs, the bound amount did not change obviously with the concentration of RF. Clearly, the imprinted Ag@SiO_2 NPs exhibited apparent affinity towards the target. A more quantitative analysis according to the Scatchard equation is shown in Fig. 4b, which gives a maximum binding capacity of 51.07 ± 2.15 nmol/g and a dissociation constant (K_d) of 0.22 ± 0.02 μM. The Scatchard plot for the RF-imprinted Ag@SiO_2 exhibited one straight line, indicating that there was only a single type of binding site between RF and the RF-imprinted NPs. Fig. 4c shows the concentration-dependent fluorescence response of the RF-imprinted Ag@SiO_2 NPs. It can be seen that the fluorescent intensity steadily increased as increasing the RF concentration. As shown in Fig. S11, the corresponding fluorescence response of non-imprinted Ag@SiO_2 NPs did not change apparently over the RF concentration range. As shown in Fig. 4d, a good linear relationship between the fluorescence intensity

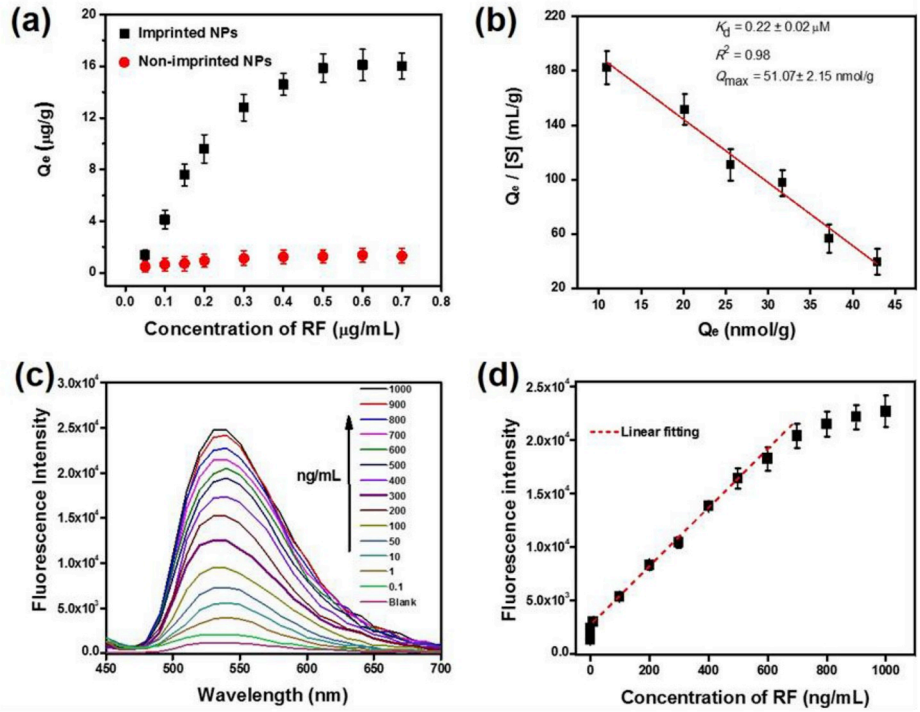

Fig. 4. (a) Binding isotherms for RF-imprinted and non-imprinted Ag@SiO_2 NPs. (b) Scatchard plot for the binding of RF-imprinted NPs with RF. (c) Concentration dependent fluorescence response of RF-imprinted Ag@SiO_2 NPs after incubation with RF of different concentrations in 100 mM phosphate buffer, pH 7.4. (d) The dependence of fluorescence intensity at 530 nm on RF concentration in solution. The excitation wavelength was set at 450 nm while the emission wavelength was set at 530 nm. Experiments were performed in triplicate; errors bars represent standard deviations. The blank signal was recorded before each set of experiments.

and RF concentration was observed in the range of 10–700 ng/mL ($I = 27.44C + 2707.47$, $R^2 = 0.998$). The developed sensing platform provided a limit of quantitation (LOQ) as 10 ± 0.5 ng/mL or 26.6 ± 1.3 nM and a limit of detection (LOD) as 3.3 ng/mL or 8.9 nM. The imprinting efficiency (IE) on RF-imprinted Ag@SiO_2 NPs was estimated to be 51%, which was excellent in molecular imprinting. Moreover, the RF-imprinted NPs exhibited fast binding equilibrium, reach equilibrium within 20 min (Fig. S12).

3.7. Cross-reactivity test

To verify the specificity, cross-reactivity of the RF-imprinted Ag@SiO_2 NPs towards a range of compounds, including the target, FMN (flavin mononucleotide, flavin-containing), VB12, VB9, VB6, nicotinamide adenine dinucleotide (NADH), tyrosine, and tryptophan, was investigated. The concentration used was 0.1 μg/mL for RF but 1 mg/mL concentrations for all the interfering species. As shown in Fig. 5, the cross-reactivity of the RF-imprinted Ag@SiO_2 NPs was low (5–7%) for most of the interfering species except FMN (20%), VB12 (11%) and VB9 (12%), which has highly similar chemical structure or unit. Therefore, the RF-imprinted Ag@SiO_2 exhibited high specificity towards the target molecule.

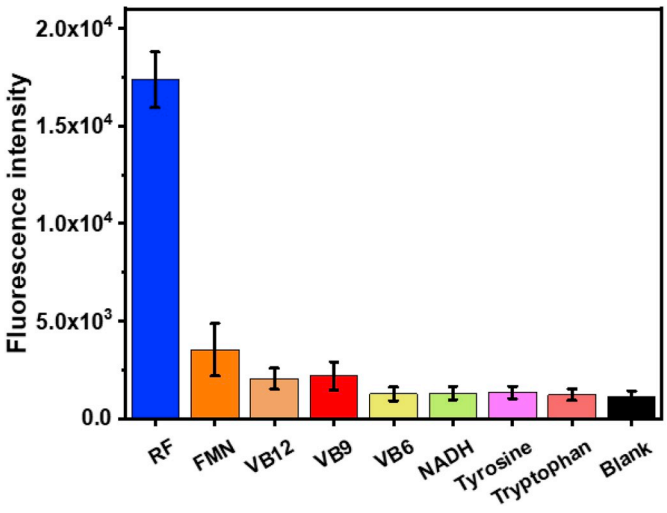

Fig. 5. Cross-reactivity test for RF-imprinted NPs against different compounds. Sample: 1 μg/mL of RF or 1 mg/mL competitive compounds dissolved in 100 mM phosphate buffer, pH 7.4. Experiments were performed in triplicate; errors bars represent standard deviations.

3.8. Method validation and detection of RF in human urine

To demonstrate feasibility of the RF-imprinted Ag@SiO_2 for real applications, the developed PEF assay was applied to the detection of RF in human urine. Given that the MIPs had high specificity toward the target, we assumed that the matrix effect could be effectively diminished, which have been demonstrated in our previous studies (Ye et al., 2014; Liu et al., 2016; Tu et al., 2016; Muhammad et al., 2017; Xing et al., 2019). Thus, we could calculate the original concentration of RF in the non-spiked urine samples according to the linear calibration curve. Based on fitted linear relationship shown in Fig. 4d, the PEF signal intensity was linearly dependent on the analyte concentration. With the measured fluorescence intensity for a urine sample from one healthy volunteer, the concentration of RF in the sample was detected as 0.40 ± 0.013 μg/mL. Moreover, to evaluate the matrix effect, we detected spiked urine samples at three concentration levels, including 20, 50 and 200 ng/mL (Table S2), and the calculated original concentration was 0.42 ± 0.032 μg/mL. There was no significant difference between the detected and calculated values *t*-test. In addition, the recovery was in the range of 96–112 %, and the relative standard deviation (RSD) was in the range of 2.4–6.7 % (Table S2).

With the measured fluorescence intensity for another three urine samples from healthy volunteers, the concentration of RF in the sample was calculated to be 0.61, 0.48 and 0.37 μg/mL, respectively, which is in good agreement with the normal range for healthy individuals (0.35–1.15 μg/mL) (Lakowicz et al., 2003; Dou et al., 2009). These results demonstrate that the nano MIP-based PEF assay was specific and

sensitive enough to provide reliable assays for complex real samples.

3.9. Comparison of this method with other methods

To comprehensively evaluate the current method, we compared this method with other methods for the quantitation of RF in human urine in terms of several respects, including sample pretreatment time, separation time, LOD, linear range and recovery (Table S3). In most of other methods, due to the lack of sensitivity and specificity, enrichment and separation steps were necessary, which not only required extra instrument but also prolonged analysis time. Compared with chromatographic or electrophoretic method, the proposed method just needs only one step to achieve separation and enrichment. Moreover, HPLC or CE take much time to precondition the column or capillary prior to separation and between runs. However. this method avoids this step, allowing for high-throughput analysis. By virtue of specific recognition of MIP, our method is straightforward, specific and highly sensitive. Currently, the linear range was not wide compared with HPLC method due to limited surface capacity of imprinted NPs. However, this issue can be easily solved by increasing the amounts of imprinted NPs used. The more the imprinting NPs used, the wider the linear range will be. Therefore, it holds great promise in real-world applications.

3.10. SERS of RF on bare AgNPs and Ag@SiO_2 surface

For a better understanding of plasmonic effects on SERS and PEF, experiments of SERS on above optimized RF-inprinted Ag@SiO_2 NPs and bare AgNPs with the same core size were carried out. Fig. S13a compares SERS spectra for RF adsorbed on these two different types of plasmonic NPs. The profiles of the spectra were almost the same, but the intensity on bare AgNPs was much higher than that on RF-imprinted Ag@SiO_2 NPs, suggesting that SERS obeys a mechanism different from PEF. We estimated E-field enhancement around a 60 nm-sized bare AgNP using the FDTD method. As shown in Fig. S13b, the highest E-field enhancement distributed at the surface of the nanoparticle, different from those on Ag@SiO_2 NPs (see Figs. 1 and 3). As compared in Fig. S13c, the E_{loc}/E_{inc} value for bare AgNPs was apparently higher than that for the RF-imprinted Ag@SiO_2 NPs. More importantly, it has been established that the enhancement factor in SERS is approximately proportional to the fourth power of the enhancement of the E-field $(E_{loc}/E_{inc})^4$(Holzmeister et al., 2014). By contrast, the enhancement factor in PEF is not so significant but more complex, being a compromise between the E-field enhancement and fluorescence quenching. This further supports the necessity of precise controlling of the spacer thickness in PEF.

4. Conclusion

We have successfully prepared a well-controlled molecularly imprinted plasmonic nanostructure for sensitive and specific PEF assay. By virtue of the hydrolysis of TEOS in ethanol phase, both the silica shell and imprinting layer were controllable, allowing for facile controlling of the structure and properties of the prepared nanostructure. The hybrid nanostructure combined two aspects of desired properties; i.e., high sensitivity of PEF detection as well as high specificity by MIP. Therefore, it provided a promising nanomaterial for sensitive and specific PEF assay. Since the boronate affinity-based controllable oriented surface imprinting approach has been well established and it can be applied to a large range of compounds, we foresee such hybrid plasmonic nanostructure can find wide applications in near future.

Declaration of competing interest

The authors declare that they have no known competing financial interests or personal relationships that could have appeared to influence the work reported in this paper.

CRediT authorship contribution statement

Hui He: Investigation, Data curation, Formal analysis, Methodology, Writing - original draft. **Pir Muhammad:** Investigation, Data curation, Formal analysis. **Zhanchen Guo:** Methodology. **Qiling Peng:** Software. **Haifeng Lu:** Validation. **Zhen Liu:** Conceptualization, Funding acquisition, Supervision, Writing - original draft, Writing - review & editing.

Acknowledgements

We acknowledge financial support from the National Natural Science Foundation of China (21425520 and 21834003) and the Program B for Outstanding PhD candidate of Nanjing University (201802B069).

Appendix A. Supplementary data

Supplementary data to this article can be found online at https://doi.org/10.1016/j.bios.2019.111733.

References

Abadeer, N.S., Brennan, M.R., Wilson, W.L., Murphy, C.J., 2014. ACS Nano 8, 8392–8406.
Adbo, K., Nicholls, I.A., 2001. Anal. Chim. Acta 435, 115–120.
Aslan, K., Gryczynski, I., Malicka, J., Matveeva, E., Lakowicz, J.R., Geddes, C.D., 2005. Curr. Opin. Biotechnol. 16, 55–62.
Bai, W., Spivak, D.A., 2014. Angew. Chem. Int. Ed. Engl. 53, 2095–2098.
Baida, H., Billaud, P., Marhaba, S., Christofilos, D., Cottancin, E., Crut, A., Lermé, J., Maioli, P., Pellarin, M., Broyer, M., 2009. Nano Lett. 9, 3463–3469.
Bardhan, R., Grady, N.K., Halas, N.J., 2008. Small 4, 1716–1722.
Bauch, M., Toma, K., Toma, M., Zhang, Q., Dostalek, J., 2014. Plasmonics 9, 781–799.
Bharadwaj, P., Novotny, L., 2007. Opt. Express 15, 14266–14274.
Bharadwaj, P., Novotny, L., 2010. J. Phys. Chem. C 114, 7444–7447.
Bhogal, S., Kaur, K., Maheshwari, S., Malik, A.K., 2019. J. Fluoresc. 29, 145–154.
Bi, X.D., Liu, Z., 2014. Anal. Chem. 86, 12382–12389.
Bie, Z.J., Chen, Y., Ye, J., Wang, S.S., Liu, Z., 2015. Angew. Chem. Int. Ed. Engl. 54, 10211–10215.
Bie, Z.J., Xing, R.R., He, X.P., Ma, Y.Y., Chen, Y., Liu, Z., 2018. Anal. Chem. 90, 9845–9852.
Brolo, A.G., Kwok, S.C., Moffitt, M.G., Gordon, R., Riordon, J., Kavanagh, K.L., 2005. J. Am. Chem. Soc. 127, 14936–14941.
Canfarotta, F., Lezina, L., Guerreiro, A., Czulak, J., Petukhov, A., Daks, A., Smolinska-Kempisty, K., Poma, A., Piletsky, S., Barlev, N.A., 2018. Nano Lett. 18, 4641–4646.
Cannone, F., Chirico, G., Bizzarri, A.R., Cannistraro, S., 2006. J. Phys. Chem. B 110, 16491–16498.
Chen, L.X., Wang, X.Y., Lu, W.H., Wu, X.Q., Li, J.H., 2016. Chem. Soc. Rev. 45, 2137–2211.
Chen, X.Q., Luan, Y., Wang, N.W., Zhou, Z.P., Ni, X.N., Cao, Y.F., Zhang, G.S., Lai, Y.F., Yang, W.M., 2018. J. Sep. Sci. 41, 4394–4401.
Chen, Y., Yin, D.Y., Ma, Y.Y., Bie, Z.J., Liu, Z., 2016. Anal. Chem. 88, 8123–8128.
Dong, Y.R., Li, W., Gu, Z.K., Xing, R.R., Ma, Y.Y., Zhang, Q., Liu, Z., 2019. Angew. Chem., Int. Ed. Engl. 58, 10621–10625.
Dostalek, J., Knoll, W., 2008. Biointerphases 3, FD12–FD22.
Dou, P., Liang, L., He, J.G., Liu, Z., Chen, H.Y., 2009. J. Chromatogr. A 1216, 7558–7563.
Gao, L., Wang, J.X., Li, X.Y., Yan, Y.S., Li, C.X., Pan, J.M., 2014. Anal. Bioanal. Chem. 406, 7213–7220.
Geddes, C.D., Lakowicz, J.R., 2002. J. Fluoresc. 12, 121–129.
Holzmeister, P., Acuna, G.P., Grohmann, D., Tinnefeld, P., 2014. Chem. Soc. Rev. 43, 1014–1028.
Kinkhabwala, A., Yu, Z., Fan, S., Avlasevich, Y., Müllen, K., Moerner, W., 2009. Nat. Photonics 3, 654.
Lakowicz, J.R., Malicka, J., D'Auria, S., Gryczynski, I., 2003. Anal. Biochem. 320, 13–20.
Lee, P., Meisel, D., 1982. J. Phys. Chem. 86, 3391–3395.
Li, H., Qiang, W., Vuki, M., Xu, D., Chen, H.-Y., 2011. Anal. Chem. 83, 8945–8952.
Li, J.F., Li, C.Y., Aroca, R.F., 2017. Chem. Soc. Rev. 46, 3962–3979.
Li, J.H., Fu, J.Q., Yang, Q., Wang, L.Y., Wang, X.Y., Chen, L.X., 2018. Analyst 143, 3570–3578.
Li, L., Lu, Y., Bie, Z.J., Chen, H.Y., Liu, Z., 2013. Angew. Chem. Int. Ed. Engl. 52, 7451–7454.
Li, M., Cushing, S.K., Wu, N., 2015. Analyst 140, 386–406.
Li, W., Zhang, Q., Wang, Y., Ma, Y., Guo, Z., Liu, Z., 2019. Anal. Chem. 91, 4831–4837.
Liu, J., Yin, D.Y., Wang, S.S., Chen, H.Y., Liu, Z., 2016. Angew. Chem. Int. Ed. Engl. 55, 13215–13218.
Liu, Z., He, H., 2017. Acc. Chem. Res. 50, 2185–2193.
Ming, T., Zhao, L., Yang, Z., Chen, H., Sun, L., Wang, J., Yan, C., 2009. Nano Lett. 9, 3896–3903.
Muhammad, P., Tu, X.Y., Liu, J., Wang, Y.J., Liu, Z., 2017. ACS Appl. Mater. Interfaces 9, 12082–12091.
Niu, C.X., Peng, M.S., You, Y., Wang, R.H., Jia, Y.J., Xie, T.X., Wang, J.Y., Na, N., Ouyang, J., 2017. Chem. Comm. 53, 5633–5636.

Park, J.-H., Byun, J.-Y., Jang, H., Hong, D., Kim, M.-G., 2017. Biosens. Bioelectron. 97, 292–298.
Punj, D., Regmi, R., Devilez, A., Plauchu, R., Moparthi, S.B., Stout, B., Bonod, N., Rigneault, H., Wenger, J.r.m., 2015. ACS Photonics 2, 1099–1107.
Schmelzeisen, M., Zhao, Y., Klapper, M., Müllen, K., Kreiter, M., 2010. ACS Nano 4, 3309–3317.
Tachibana, S., 1971. Isolation of Riboflavin Glycosides. Methods in Enzymology. Elsevier, pp. 413–416.
Tian, J.H., Bai, J.L., Peng, Y., Qie, Z.W., Zhao, Y.F., Ning, B.A., Xiao, D., Gao, Z.X., 2015. Analyst 140, 5301–5307.
Ton, X.A., Bui, B.T.S., Resmini, M., Bonomi, P., Dika, I., Soppera, O., Haupt, K., 2013. Angew. Chem. Int. Ed. Engl. 52, 8317–8321.
Touahir, L., Galopin, E., Boukherroub, R., Gouget-Laemmel, A.C., Chazalviel, J.-N., Ozanam, F., Szunerits, S., 2010. Biosens. Bioelectron. 25, 2579–2585.
Tu, X.Y., Muhammad, P., Liu, J., Ma, Y.Y., Wang, S.S., Yin, D.Y., Liug, Z., 2016. Anal. Chem. 88, 12363–12370.
Vlatakis, G., Andersson, L.I., Muller, R., Mosbach, K., 1993. Nature 361, 645–647.
Volpati, D., Job, A.E., Aroca, R., Constantino, C., 2008. J. Phys. Chem. B 112, 3894–3902.
Wan, W., Biyikal, M., Wagner, R., Sellergren, B., Rurack, K., 2013. Angew. Chem. Int. Ed. Engl. 52, 7023–7027.
Wang, J.F., Cormack, P.A.G., Sherrington, D.C., Khoshdel, E., 2003. Angew. Chem. Int. Ed. Engl. 42, 5336–5338.
Wang, S.S., Ye, J., Bie, Z.J., Liu, Z., 2014. Chem. Sci. 5, 1135–1140.
Wang, S.S., Yin, D.Y., Wang, W.J., Shen, X.J., Zhu, J.J., Chen, H.Y., Liu, Z., 2016. Sci. Rep. 6.
Wang, X.Y., Yu, S.M., Liu, W., Fu, L.W., Wang, Y.Q., Li, J.H., Chen, L.X., 2018. ACS Sens. 3, 378–385.
Whitcombe, M.J., Chianella, I., Larcombe, L., Piletsky, S.A., Noble, J., Porter, R., Horgan, A., 2011. Chem. Soc. Rev. 40, 1547–1571.
Xing, R.R., Ma, Y.Y., Wang, Y.J., Wen, Y.R., Liu, Z., 2019. Chem. Sci. 10, 1831–1835.
Xing, R.R., Wang, S.S., Bie, Z.J., He, H., Liu, Z., 2017. Nat. Protoc. 12, 964–987.
Xu, Z., Chen, Y., Gartia, M.R., Jiang, J., Liu, G.L., 2011. Appl. Phys. Lett. 98, 241904.
Yang, Q., Li, J.H., Wang, X.Y., Peng, H.L., Xiong, H., Chen, L.X., 2018. Biosens. Bioelectron. 112, 54–71.
Ye, J., Chen, Y., Liu, Z., 2014. Angew. Chem. Int. Ed. Engl. 53, 10386–10389.
Ye, L., Mosbach, K., 2001. J. Am. Chem. Soc. 123, 2901–2902.
Yin, D.Y., Li, X.L., Ma, Y.Y., Liu, Z., 2017. Chem. Comm. 53, 6716–6719.
Yin, D.Y., Wang, S.S., He, Y.J., Liu, J., Zhou, M., Ouyang, J., Liu, B.R., Chen, H.Y., Liu, Z., 2015. Chem. Comm. 51, 17696–17699.
Zhou, W., Huang, P.-J.J., Ding, J., Liu, J., 2014. Analyst 139, 2627–2640.
Zhou, Z., Huang, H., Chen, Y., Liu, F., Huang, C.Z., Li, N., 2014. Biosens. Bioelectron. 52, 367–373.